

Structural Origin of Suppressed Voltage Decay in Single-Crystalline Li-Rich Layered $\text{Li}[\text{Li}_{0.2}\text{Ni}_{0.2}\text{Mn}_{0.6}]\text{O}_2$ Cathodes

Xiaoxia Yang, Suning Wang, Duzhao Han, Kai Wang, Akhil Tayal, Volodymyr Baran, Alexander Missyul, Qiang Fu, Jiangxuan Song, Helmut Ehrenberg, Sylvio Indris, and Weibo Hua*

Lithium- and manganese-rich layered oxides (LMLOs, $\geq 250 \text{ mAh g}^{-1}$) with polycrystalline morphology always suffer from severe voltage decay upon cycling because of the anisotropic lattice strain and oxygen release induced chemo-mechanical breakdown. Herein, a Co-free single-crystalline LMLO, that is, $\text{Li}[\text{Li}_{0.2}\text{Ni}_{0.2}\text{Mn}_{0.6}]\text{O}_2$ (LLNMO-SC), is prepared via a Li^+/Na^+ ion-exchange reaction. In situ synchrotron-based X-ray diffraction (sXRD) results demonstrate that relatively small changes in lattice parameters and reduced average micro-strain are observed in LLNMO-SC compared to its polycrystalline counterpart (LLNMO-PC) during the charge–discharge process. Specifically, the as-synthesized LLNMO-SC exhibits a unit cell volume change as low as 1.1% during electrochemical cycling. Such low strain characteristics ensure a stable framework for Li-ion insertion/extraction, which considerably enhances the structural stability of LLNMO during long-term cycling. Due to these peculiar benefits, the average discharge voltage of LLNMO-SC decreases by only $\approx 0.2 \text{ V}$ after 100 cycles at 28 mA g^{-1} between 2.0 and 4.8 V, which is much lower than that of LLNMO-PC ($\approx 0.5 \text{ V}$). Such a single-crystalline strategy offers a promising solution to constructing stable high-energy lithium-ion batteries (LIBs).

electric vehicles (HEVs), next-generation lithium-ion batteries (LIBs) that utilize high-energy cathode materials are crucially needed.^[1–3] Among various types of cathode materials, Li- and Mn-rich layered oxides (LMLOs) are regarded as one of the most promising cathode candidates owing to their high capacity ($\geq 250 \text{ mAh g}^{-1}$) and low cost.^[4–7] The high capacity of LMLOs is widely believed to originate predominantly from the reversible cationic and anionic redox activities,^[8–10] which remarkably overcome the capacity limitations of conventional cathode materials ($< 200 \text{ mAh g}^{-1}$) like olivine LiFePO_4 (space group: $Pnma$),^[11,12] spinel LiMn_2O_4 ($Fd\bar{3}m$),^[13,14] and layered $\text{Li}[\text{Ni},\text{Co},\text{Mn}]\text{O}_2$ (NCM, square brackets represent transition metal ions located on octahedral positions, $R\bar{3}m$)^[15–18] because of the sole transition metal (TM) redox activity in these cathodes. Nevertheless, LMLOs always undergo a severe voltage decay upon cycling,^[19,20] which seriously hinders


1. Introduction

To meet the ever-increasing requirements for electrical energy storage devices such as electric vehicles (EVs) and hybrid

the practical application of LMLOs. Over the last two decades, a series of attempts have been made to reveal the underlying structural degradation mechanism and mitigate the voltage decay during extended cycling.

X. Yang, S. Wang, D. Han, W. Hua
School of Chemical Engineering and Technology
Xi'an Jiaotong University
No.28, West Xianning Road, Xi'an 710049, China
E-mail: weibo.hua@xjtu.edu.cn

S. Wang, Q. Fu, H. Ehrenberg, S. Indris, W. Hua
Institute for Applied Materials (IAM)
Karlsruhe Institute of Technology (KIT)
Hermann-von-Helmholtz-Platz 1
D-76344 Eggenstein-Leopoldshafen, Germany

 The ORCID identification number(s) for the author(s) of this article can be found under <https://doi.org/10.1002/smll.202201522>.

© 2022 The Authors. Small published by Wiley-VCH GmbH. This is an open access article under the terms of the Creative Commons Attribution-NonCommercial License, which permits use, distribution and reproduction in any medium, provided the original work is properly cited and is not used for commercial purposes.

K. Wang
Institute of Nanotechnology (INT)
Karlsruhe Institute of Technology (KIT)
76344 Eggenstein-Leopoldshafen, Germany

A. Tayal, V. Baran
Deutsches Elektronen-Synchrotron (DESY)
Notkestr. 85, 22607 Hamburg, Germany

A. Missyul
CELLS-ALBA Synchrotron
Cerdanyola del Valles, Barcelona E-08290, Spain

J. Song
State Key Laboratory for Mechanical Behavior of Materials
School of Materials Science and Engineering
Xi'an Jiaotong University
No. 28 Xianning West Road, Xi'an 710049, China

DOI: 10.1002/smll.202201522

The irreversible Li/O loss-induced surface/bulk phase transformation has been reported as one of the main causes of voltage degradation in LMLOs.^[4,5] Previous studies^[21,22] have suggested that the atomic rearrangements at the LMLO surface, that is, the phase transition from layered to spinel/rock-salt structure, are more likely to take place, and then progressively propagate into the inner bulk part of the crystallites during high-voltage cycling (4.8 V). Moreover, our group^[7] found that there was an increase in tensile strain from the core to the surface region of $\text{Li}[\text{Li}_{0.2}\text{Ni}_{0.2}\text{Mn}_{0.6}]\text{O}_2$ (LLNMO) crystallites after 1 year cycling. Thereby, the particle morphology and size distribution significantly affect the electrochemical performance of Li-rich cathode materials. Generally, the layered transition metal oxides, including NCM and LMLOs, are synthesized by using a co-precipitation method followed by a high-temperature solid-state reaction.^[23–27] The nano-sized primary particles tend to agglomerate to form micron-sized spherical secondary particles during the co-precipitation process, concomitant with the formation of voids inside the secondary particles.^[28,29] The agglomerates provide a reduced diffusion length for Li-ions within their primary particles and an increased number of pores, which facilitate the transport of Li-ions and enhance the rate capability of cathode materials. Thus, these spherical polycrystalline particles have become the most popular morphology for both traditional NCM and LMLO cathodes.^[30–32] However, the inhomogeneous volume change of primary particle and the anisotropic lattice strain in individual grains inside the polycrystalline particles over cycling enhance cracking along the weak internal grain boundaries and pulverization.^[32–34] Furthermore, the oxygen release from the crystal lattice of LMLOs contributes to the crack formation and the generation of large pores within particles.^[35–37] These intergranular fractures expose new surfaces to the electrolyte prone to side reactions, accelerating the voltage fade and capacity deterioration of LMLOs.^[38] Single-crystalline LMLO cathodes are expected to have great potential to address this issue by decreasing the surface area and the number of phase boundaries.^[3] Unfortunately, the synthesis of high-performance single-crystalline LMLO electrode materials results in additional challenges since the path length for Li-ion transport is increased.

Na-containing compounds have recently been used to convert them into well-designed Li-containing compounds by exchange of Na-ions for Li-ions.^[39,40] The Li^+/Na^+ ion-exchange reaction is a type of chemical reaction in which Na-containing substances react with Li salt solutions to selectively remove Na-ions and replace them with Li-ions from the solution.^[41] As a consequence, the obtained Li-containing materials possess a crystallographic structure, particle morphology, and size similar to their Na analogues. Inspired by the motives described above, this work uses single-crystalline layered $\text{Na}_{2/3}[\text{Ni}_{0.25}\text{Mn}_{0.75}]\text{O}_2$ as a starting material to controllably synthesize Co-free Li-rich layered $\text{Li}[\text{Li}_{0.2}\text{Ni}_{0.2}\text{Mn}_{0.6}]\text{O}_2$ single crystals (LLNMO-SC). We carry out a systematic study on the crystal structure, morphology, and electrochemistry of LLNMO-SC and its polycrystalline (LLNMO-PC) counterpart by combining synchrotron-based X-ray diffraction (sXRD) and X-ray absorption spectroscopy (XAS) with high penetration depth and the capability to obtain average information on the whole cathode, transmission electron microscopy (TEM) with atomic-level spatial resolution, and electrochemical

tests. As a cathode material in a LIB, LLNMO-SC achieves an outstanding cycling performance with both capacity and energy retention of nearly 100% after 100 cycles, whereas LLNMO-PC shows a serious capacity fade with 95% capacity retention and 86% energy retention at 0.1 C (28 mA g⁻¹) between 2.0 and 4.8 V. Comparison of the discharge-voltage profiles of LLNMO-SC and LLNMO-PC reveals that the regulation of the particle size is quite effective in order to suppress the voltage decay of LLNMO during extended cycling. A large number of in situ and ex situ sXRD and XAS results were acquired to study the structural origin of enhanced cycling performance and suppressed voltage decay of LLNMO-SC on different length scales.

2. Results and Discussion

For comparison, LLNMO-PC was prepared through traditional hydroxide coprecipitation and solid-state reaction, as shown in **Figure 1a**. For the synthesis of LLNMO-SC, single-crystalline layered $\text{Na}_{2/3}[\text{Ni}_{0.25}\text{Mn}_{0.75}]\text{O}_2$ with the P2 structure ($P6_3/mmc$) was firstly obtained via conventional high-temperature solid-state reaction. The prepared $\text{Na}_{2/3}[\text{Ni}_{0.25}\text{Mn}_{0.75}]\text{O}_2$ was thoroughly mixed with 10% excess of $\text{LiOH}\cdot\text{H}_2\text{O}$, and the mixture was calcined at 900 °C for 12 h to obtain LLNMO-SC. Details of the synthesis procedure are given in the Supplementary Information. An inductively coupled plasma mass spectrometer (ICP-MS) was conducted to determine the accurate chemical compositions of LLNMO-SC and LLNMO-PC. The atomic ratio of Li, Ni, and Mn for both LLNMO-SC and LLNMO-PC is close to 1.2:0.2:0.6, which is consistent with the theoretical ratio of elements in $\text{Li}[\text{Li}_{0.2}\text{Ni}_{0.2}\text{Mn}_{0.6}]\text{O}_2$, as shown in Table S1 (Supporting Information).

LLNMO-PC is composed of typical secondary particles of around 2 μm in size that are agglomerated with platelet-like nanosheets with a lateral dimension of about 300 nm, as displayed in scanning electron microscopy (SEM) (Figure 1b [inset]; and Figure S1a,c, Supporting Information) and transmission electron microscopy (TEM) images (Figure S2a, Supporting Information). In contrast to LLNMO-PC, LLNMO-SC consists of polyhedral brick-like shape crystals with the primary particle size distribution ranging from 1 to 2 μm, see Figure 1c (inset), and Figures S1b,d and S2b (Supporting Information). SEM–energy dispersive-spectroscopy (EDS) mapping reveals that Ni, Mn, and O were uniformly distributed in the LLNMO-SC, as shown in Figure S3 (Supporting Information). The corresponding element contents of Mn and Ni are around 73 and 27 wt.%, respectively, see Table S2 (Supporting Information). All the reflections in the synchrotron-based X-ray diffraction (sXRD) patterns of both samples can be well assigned according to a single monoclinic layered phase with space group $C2/m$, and no impurity phases were found. Rietveld refinements were performed by assuming a layered structure with the structural model $[\text{Li}][\text{Li}_{0.2}\text{Ni}_{0.2}\text{Mn}_{0.6}]\text{O}_2$, and the reasonably small weighted profile R -factor, R_{wp} , indicates that the fitting results are reliable (see Tables S3 and S4, Supporting Information). Rietveld refinement against the sXRD pattern of LLNMO-SC yields lattice parameters of $a = 4.9616$ (2) Å, $b = 8.5801$ (3) Å, $c = 5.0354$ (5) Å, and $\beta = 109.3231$ (2)°, which are similar to the lattice parameters of LLNMO-PC and in good agreement with

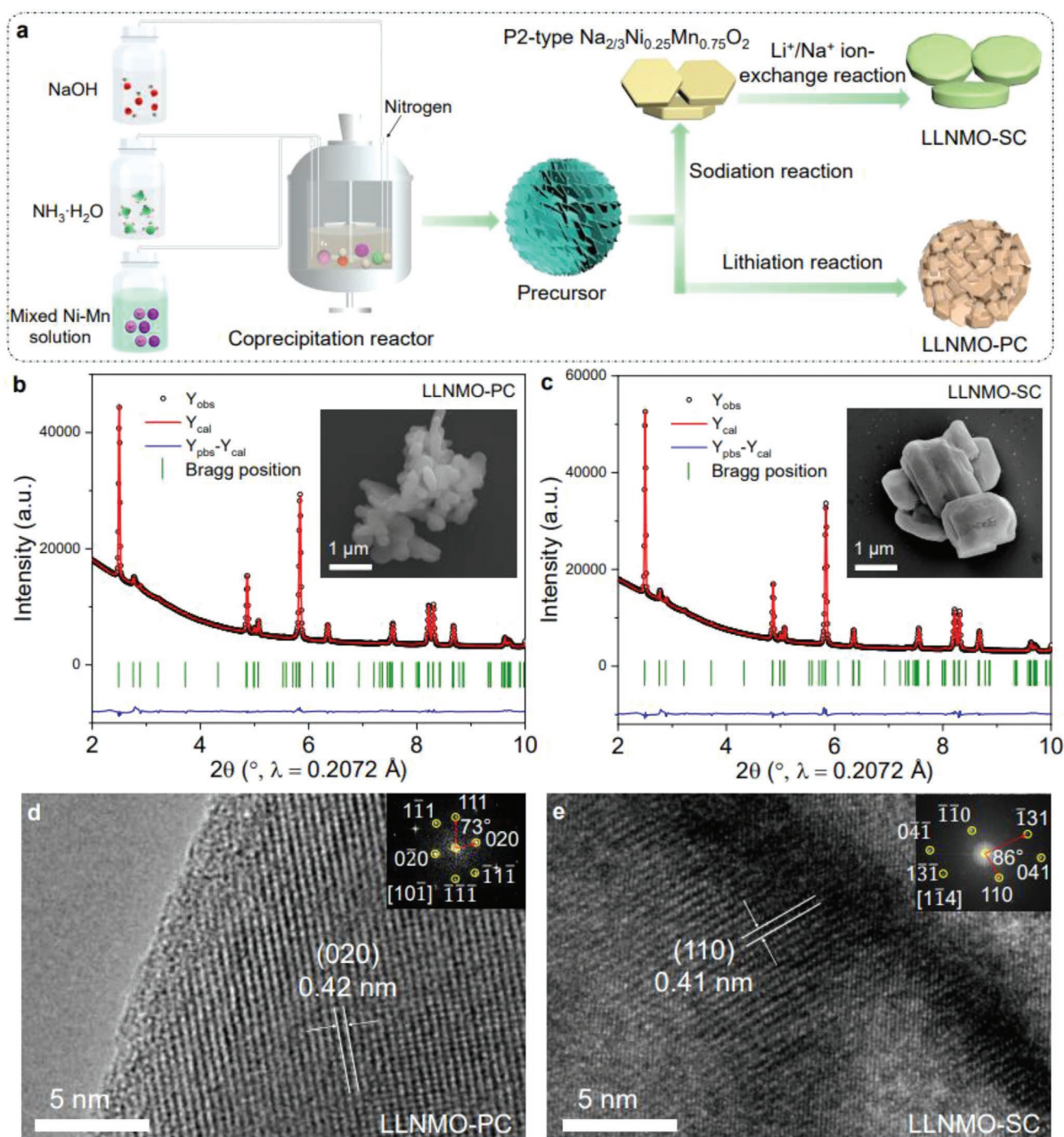


Figure 1. a) Schematic diagram of the synthesis of polycrystalline and single-crystalline $\text{Li}[\text{Li}_{0.2}\text{Ni}_{0.2}\text{Mn}_{0.6}]\text{O}_2$ cathode materials; the xSRD patterns and corresponding Rietveld refinement results of b) LLNMO-PC and c) LLNMO-SC, the corresponding SEM images are shown in the inset; the HRTEM images and corresponding FFT patterns (inset) of d) LLNMO-PC and e) LLNMO-SC.

the data published previously.^[7,42] The high-angle annular dark-field scanning TEM (HAADF-STEM)–EDS mapping results indicate that the Ni, Mn, and O elements are homogeneously distributed in the selected area of LLNMO-PC (Figure S4, Supporting Information). Interestingly, most of the sodium ions are located on the surface of the crystallites after the ion-exchange reaction before washing (see Figure S5, Supporting

Information), revealing that the Na-ions in the P2-type layered $\text{Na}_{2/3}[\text{Ni}_{0.25}\text{Mn}_{0.75}]\text{O}_2$ ($P6_3/mmc$, Figure S6, Supporting Information) were successfully replaced by Li-ions and Na compounds are formed in the near-surface region of the oxides. These Na species would be removed after water-washing treatment (see Figures S7 and S8, Supporting Information). The atomic ratio of Ni and Mn detected from the EDX spectrum is close

to 1:3 for both LLNMO-PC and LLNMO-SC (Tables S5 and S6, Supporting Information), which agrees reasonably well with the designed chemical formula of $\text{Li}[\text{Li}_{0.2}\text{Ni}_{0.2}\text{Mn}_{0.6}]\text{O}_2$. The high-resolution TEM (HRTEM) image (Figure 1d) of LLNMO-PC shows clear lattice fringes with an average interplanar spacing of approximately 0.42 nm that can be indexed to the (020) plane of the monoclinic layered structure ($C2/m$). The corresponding Fast Fourier Transform (FFT) patterns along the [101] zone axis in Figure 1d exhibit an array of points with hexagonal symmetry, revealing that these particles possess a layered structure. Figure 1e shows the HRTEM image of LLNMO-SC, and the measured average d -spacing is approximately 0.41 nm, corresponding to the d value of (110) plane of monoclinic layered LLNMO. The FFT patterns along the [114] zone axis are consistent with a space group symmetry of $C2/m$, confirming that the selected crystals are single-crystalline.

The electrochemical characteristics of LLNMO-PC and LLNMO-SC electrodes were measured in CR2032-type coin cells between 2.0 and 4.8 V (vs Li/Li⁺) at a current density of 0.1 C (1 C = 280 mA g⁻¹). Figure S9 (Supporting Information) presents the first and second charge–discharge voltage curves of LLNMO-PC and LLNMO-SC cathodes at room temperature. The initial charge profile of the LLNMO-PC electrode shows a monotonic sloping region below 4.5 V and a high-voltage plateau at around 4.6 V versus Li/Li⁺, which generally can be ascribed to the oxidation of Ni²⁺ to Ni⁴⁺ and O²⁻ to O^{*n-*} ($0 < n < 2$), respectively, in good accordance with previously reported profiles of layered LLNMO with polycrystalline morphology.^[6,20] In contrast to the LLNMO-PC cathode, the plateau ascribed to oxygen redox activity occurs at about 4.7 V in the LLNMO-SC cathode, which is different from the typical polycrystalline Li-rich layered cathode materials.^[19,35] The initial specific discharge capacity of the LLNMO-SC electrode is around 155 mAh g⁻¹ (corresponding to about 0.5 Li-ion extraction from LLNMO-SC), which is lower than that of the LLNMO-PC electrode (about 200 mAh g⁻¹, 0.6 Li-ion deintercalation from LLNMO-PC). This is probably due to the sluggish Li-ion diffusion kinetics in single-crystalline materials (see the results of electrical impedance spectroscopy in Figure S10 and Table S7, Supporting Information). Moreover, the lattice oxygen oxidation in LLNMO-SC contributes a lower specific capacity of about 117 mAh g⁻¹ compared to LLNMO-PC (≈148 mAh g⁻¹). These results reveal that a comparably strong electrochemical driving force is required to achieve the oxidation of oxygen non-bonding states in LLNMO-SC. Figure 2a shows the discharge voltage curves of LLNMO-PC and LLNMO-SC electrodes for the initial and selected cycles. An increase in the specific discharge capacity of the LLNMO-SC cathode with the increasing cycle number is observed. Starting at a value of 155 mAh g⁻¹ in the initial discharge, the discharge specific capacity increases by about 30% to a value of 201 mAh g⁻¹ after 15 cycles. Nearly 100% of the specific discharge capacity of the LLNMO-SC electrode can then be maintained for the subsequent 85 cycles. Most importantly, negligible discharge voltage decay is obviously found in the LLNMO-SC electrode during the 100 cycles. Specifically, the average voltages of the LLNMO-SC electrode for the 1st, 10th, 20th, 50th, 70th, and 100th discharge processes are 3.72, 3.69, 3.64, 3.56, 3.52, and 3.47 V, respectively. The outstanding voltage retention of the LLNMO-SC electrode is in

sharp contrast to that of the LLNMO-PC electrode (i.e., 3.70, 3.61, 3.55, 3.37, 3.27, and 3.21 V for the 1st, 10th, 20th, 50th, 70th, and 100th discharge). The corresponding dQ/dV plots of both electrodes are displayed in Figure 2b. A pronounced downshift in both high-voltage (≈4.3 V) and low-voltage (≈3.1 V) regions is detected for the LLNMO-PC electrode during electrochemical cycling. In contrast, the discharge voltage fade of the LLNMO-SC electrode is apparently highly suppressed. A comparison of the cycling stability of two electrodes is shown in Figure 2b and Tables S8 and S9 (Supporting Information). After 100 cycles, the discharge capacity of the LLNMO-SC electrode (211 mAh g⁻¹) is slightly higher than that of the LLNMO-PC electrode (190 mAh g⁻¹), while the energy density of the LLNMO-SC electrode (738 Wh kg⁻¹) is highly superior to that of the LLNMO-PC electrode (612 Wh kg⁻¹) because of the mitigated voltage decay.

To figure out the reason why the LLNMO-SC electrode delivers excellent cycling stability between 2.0 and 4.8 V, in situ high-resolution sXRD was conducted for both the LLNMO-PC/Li cell and the LLNMO-SC/Li cell during galvanostatic cycling. In order to clearly illustrate the structural evolution, the contour profiles of the intensity and position for 001, 130, 133, and 331 reflections as a function of reaction time during the first cycle and the second charge process are exhibited in Figure 3a,c. Only changes in position and intensity of the Bragg reflections are observed for both electrodes, revealing a typical solid solution reaction mechanism for the monoclinic layered $\text{Li}[\text{Li}_{0.2}\text{Ni}_{0.2}\text{Mn}_{0.6}]\text{O}_2$ ($C2/m$). According to the crystal structure,^[7] the 001 and 133 reflections are sensitive to the structural changes along the c -axis, while the 130 and 331 reflections strongly reflect the evolution along the a - and b -axis of the monoclinic layered LLNMO ($C2/m$). Upon the first charging process, the 001 and 133 reflections of LLNMO-PC progressively shift to lower scattering angles as the potential increases to around 4.5 V and they move slightly back to higher 2-theta angles when the LLNMO-PC electrode is charged to 4.8 V. Meanwhile, the 130 and 331 reflections of LLNMO-PC move to higher scattering angles with the potential increasing to 4.5 V and remain almost unchanged in the voltage window of 4.5–4.8 V. This is in good agreement with a monotonous charging process in the range from open-circuit voltage to 4.5 V and a pronounced voltage plateau (lattice oxygen oxidation process) at approximately 4.6 V during the initial charge. All the reflections of the LLNMO-PC electrode tend to shift back to their primary positions during the process of initial relithiation (discharge). Upon the subsequent second charging, these reflections exhibit a symmetrical change to the first discharge, and no obvious activation process can be found. In contrast, the changes in the reflections of the LLNMO-SC cathode are basically similar to those of the LLNMO-PC cathode after the first charge (Figure 3c).

Each in situ sXRD pattern of the two electrodes during electrochemical cycling was fitted using Rietveld refinement with the structure model of $\text{Li}[\text{Li}_{0.2}\text{Ni}_{0.2}\text{Mn}_{0.6}]\text{O}_2$ ($C2/m$), see Figures S11 and S12 (Supporting Information). The obtained lattice parameters are presented in Figure 4a,b. From open-circuit voltage to 4.5 V, the parameter c of the LLNMO-PC electrode increases from 5.03(2) to 5.06(2) Å, which is attributed to an increased average distance of TM–TM interplane as

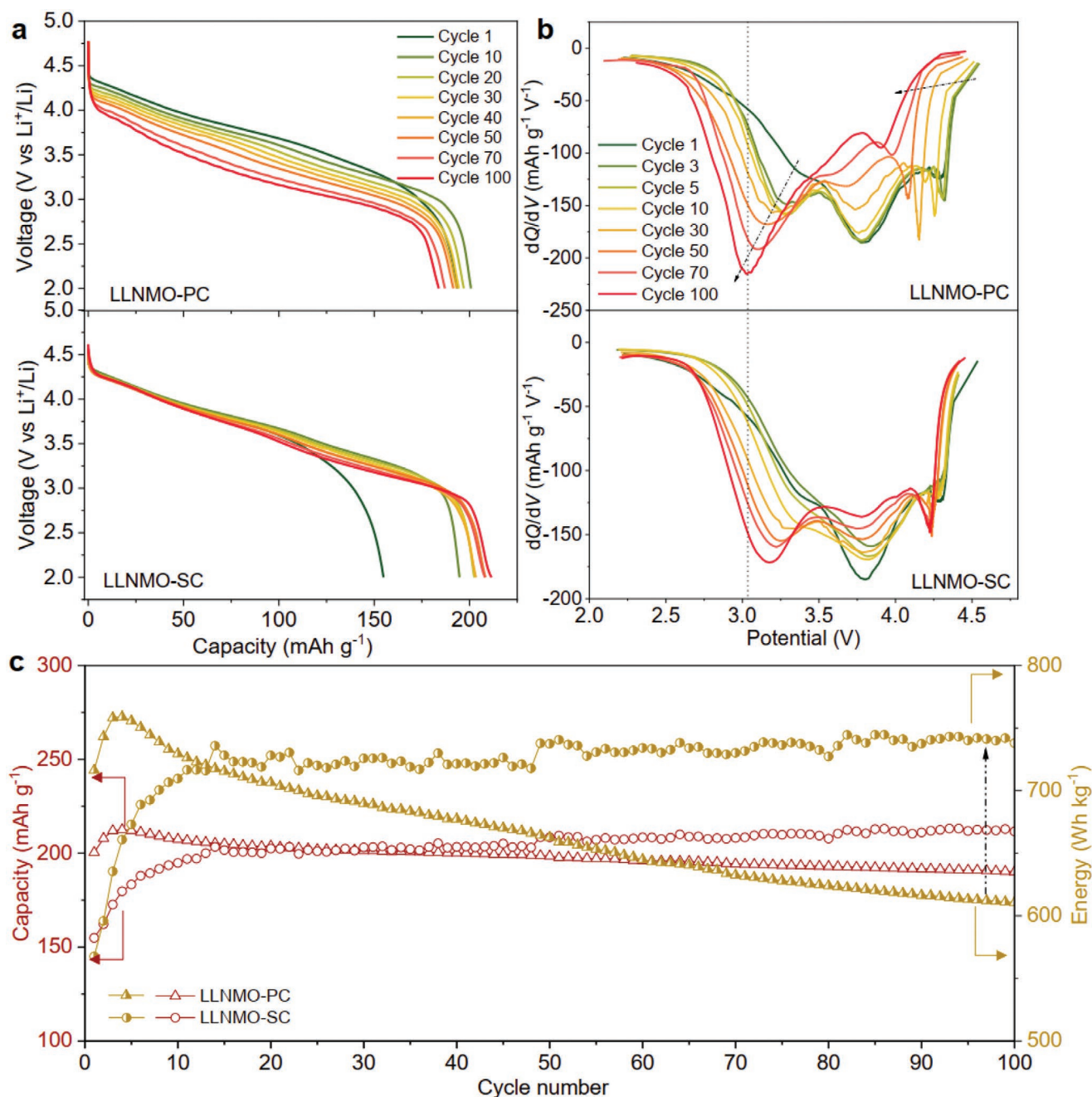


Figure 2. a) The discharge voltage curves of LLNMO-PC and LLNMO-SC electrodes for 100 cycles; b) the corresponding dQ/dV profiles of LLNMO-PC and LLNMO-SC electrodes, the arrow in the plots of LLNMO-PC highlights the profound shift towards low voltages (i.e., voltage decay) over cycling; c) comparison of specific discharge capacity and energy density retention for LLNMO-PC and LLNMO-SC electrodes cycled between 2.0 and 4.8 V at 25 °C.

a result of a decreased number of Li ions in the Li layer and an increased electrostatic repulsive force within the cubic-close packed (ccp) oxygen framework of LLNMO-PC. Simultaneously, the parameter a of the LLNMO-PC electrode decreases from 4.96(2) to 4.92(2) Å, and the parameter b is reduced from 8.58(3) to 8.52(3) Å, respectively. The shrinkage of both a and b parameters is linked to the contraction of the average TM–TM intra-plane distance, which is supposed to be caused by the smaller radii of Ni ions at higher oxidation states (i.e., Ni²⁺ → Ni⁴⁺ + 2e⁻,

see the in situ XAS results below). As the potential further increases to 4.8 V, a slight decrease in parameter c from 5.06 (2) to 5.04 (2) Å is observed, whereas the a and b parameters do not change considerably with the electrochemical extraction of more Li-ions from LLNMO-PC (i.e., Li_{1.2-x}Ni_{0.2}Mn_{0.6}O₂, 0.4 < x < 1.2). This phenomenon is probably ascribed to the reduction of the electrostatic repulsive force between oxygen–oxygen layers along the c -axis resulting from the generation of oxygen vacancy^[35] or peroxy-like O₂⁻ (1 ≤ n ≤ 3) dimers^[21] or

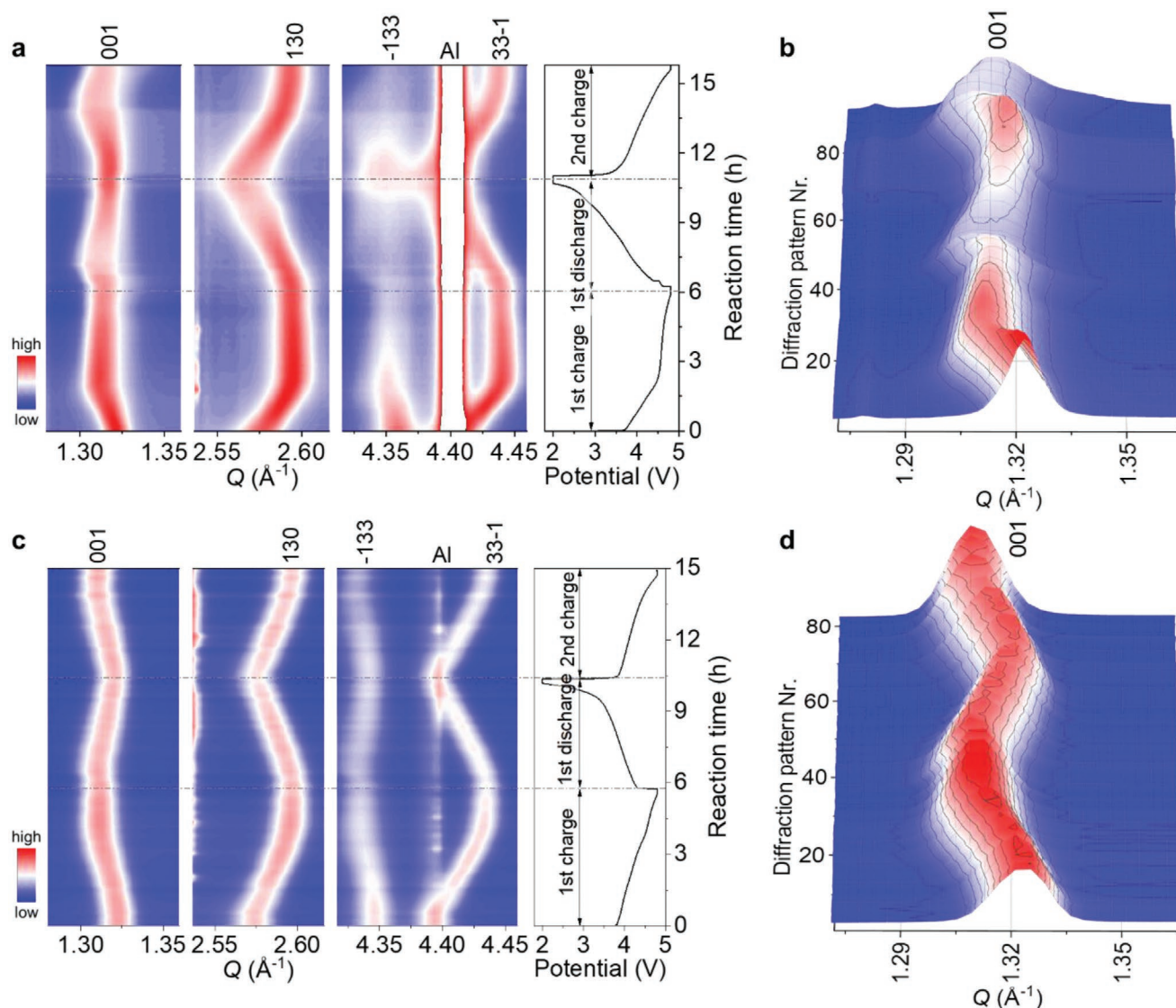


Figure 3. In situ sXRD patterns of a,b) LLNMO-PC ($\lambda = 0.4129 \text{ \AA}$) and c,d) LLNMO-SC ($\lambda = 0.2072 \text{ \AA}$) electrodes during the first cycle and the second charge. Contour maps of reflection evolution of 001, 130, 133, and 331 of a) LLNMO-PC and c) LLNMO-SC electrodes, one of the aluminum current collectors is marked in the figure.

molecular O_2 ,^[43] the localization of O 2p electron holes,^[44] and the TM migration.^[20] In contrast to LLNMO-PC, the parameter c of the LLNMO-SC electrode increases from 5.04 (2) to 5.07 (2) \AA up to the voltage of 4.5 V and remains nearly constant beyond 4.5 V, demonstrating the structural stability of LLNMO-SC in the high-voltage region (4.5–4.8 V).

Upon the first discharge, the lattice parameter c of both electrodes increases rapidly and then declines gradually, whereas the parameters of both a and b raise successively. The difference in lattice parameters of a , b , c and unit cell volume (V) of the LLNMO-SC electrode before and after the first cycle is 0.0012 (2) \AA , 0.0039 (3) \AA , 0.0104 (2) \AA , and 0.3441 (6) \AA^3 , respectively, which is much smaller than those of the LLNMO-PC electrode (i.e., 0.0112 (2) \AA , 0.0189 (3) \AA , 0.0221 (2) \AA , and 1.4018 (6) \AA^3). These results provide strong evidence for the superior structural reversibility and stability of the LLNMO-SC

electrode during cycling. A relatively small change in lattice parameters of the LLNMO-SC electrode is also supposed to be related to the low specific capacity of the LLNMO-SC electrode during the first cycle. It is found that the irreversible structural changes of LLNMO electrodes mainly occurred during the first Li-ion intercalation/de-intercalation process.^[15] Large variations in the layered structure of LLNMO-PC cathode would result in a decrease in the specific capacity during subsequent cycles (see Figure 2) and trigger a severe structural degradation during prolonged cycling (see the discussion below). During the second charging process, the lattice parameter c of the LLNMO-PC electrode decreases significantly from 5.075 (2) at ≈ 4.3 V to 5.053 (2) \AA at 4.8 V, implying a severe structural “collapse” in the c -axis in the high-voltage regime (>4.5 V). However, there is no dramatic change in the lattice parameter c of the LLNMO-SC electrode upon deep delithiation to a high

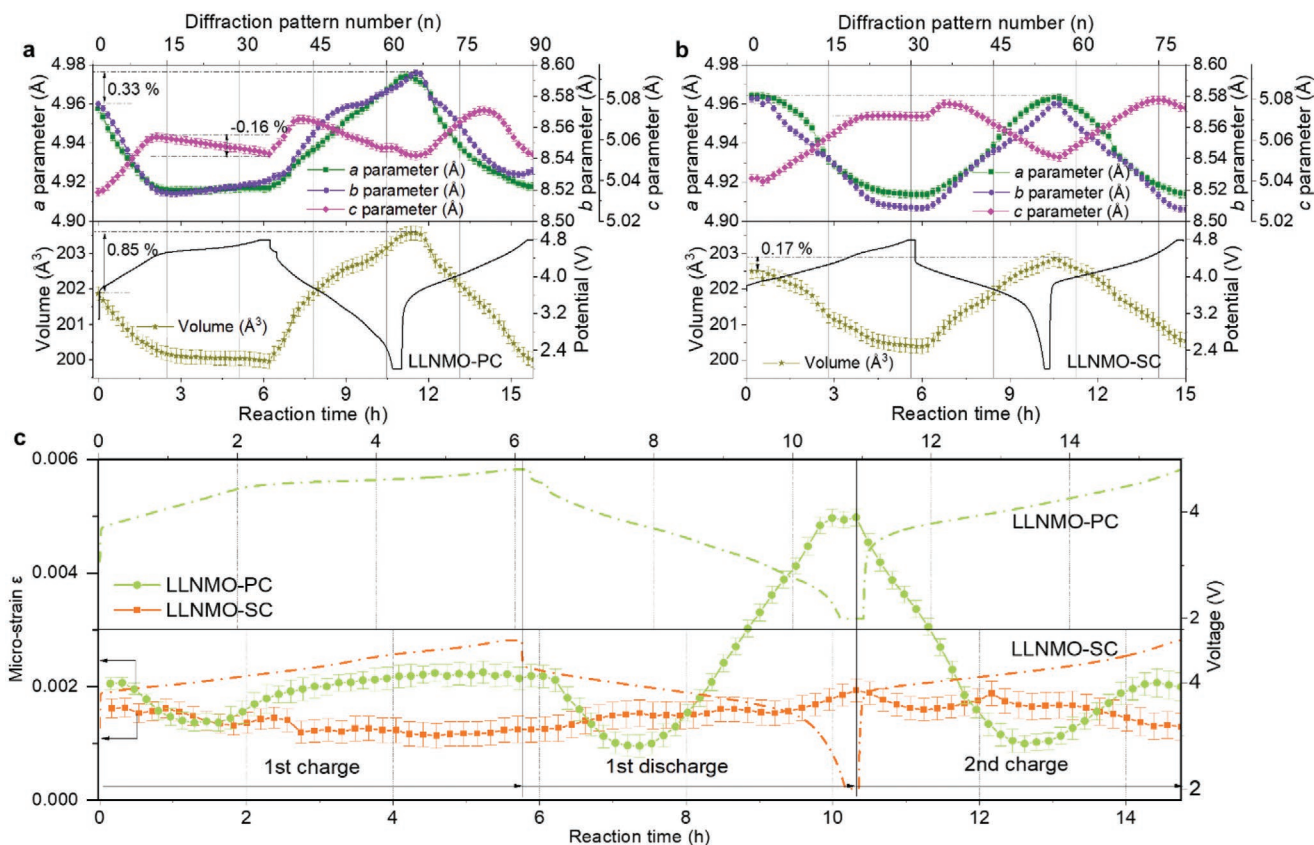


Figure 4. Changes of lattice parameters (a , b , c , and V) for a) LLNMO-PC and b) LLNMO-SC electrodes during cycling; c) the micro-strain (ϵ) analysis of both electrodes.

cut-off voltage of 4.8 V (from 5.075 (2) at ≈ 4.3 V to 5.076 (2) Å at 4.8 V).

The LLNMO-SC attains ultra-small cell volume change (about 1.1%) during insertion and extraction of Li-ion, which is smaller than that of LLNMO-PC (2.5%) and reported LLNMO cathodes.^[5,45] These results again prove the robust structural stability of the LLNMO-SC cathode and thus leading to an excellent cycling behavior as shown in Figure 2. Figure 4c depicts the micro-strain ϵ ($\Delta d/d$) of both electrodes during cycling obtained by Rietveld refinement. It is obvious that there is some variation in the lattice strain ϵ of LLNMO-PC upon delithiation/lithiation. The parameter ϵ of LLNMO-SC does not change noticeably over cycling in comparison to that of LLNMO-PC, suggesting that the microstructure of the single-crystalline Li-rich cathode is more relaxed during Li insertion/extraction compared to its polycrystalline counterpart. These small changes in the lattice strain during electrochemical cycling might be another major contribution to the mitigation of voltage decay in the LLNMO-SC electrode.

In order to explore the changes in the electronic configuration and local structure of both cathode materials, in situ XAS experiments were performed on both the LLNMO-PC/Li cell and the LLNMO-SC/Li cell during delithiation/lithiation between 2.0 and 4.8 V under a constant current of 28 mA g⁻¹. Figure 5a,f show the first charge voltage profiles and the corresponding number of XAS scans for both electrodes. In general, the X-ray absorption near-edge structure (XANES) region

of the XAS spectra of 3d transition metal oxides is closely tied to the valence state and local symmetry of TM ions, while the extended X-Ray absorption fine structure (EXAFS) region of the spectra is strongly related to the local environment of the absorber atom.^[46] The pre-edge peak in XANES spectra reflects the dipole-forbidden 1s \rightarrow 3d electronic transition of TM elements. Such a peak is usually weak for absorbers in a centrosymmetric environment (e.g., ideal octahedral sites) and it becomes more intense when the 3d and 4p orbitals hybridize owing to the non-centrosymmetric environment (e.g., tetrahedral sites) or the local structural distortion between TM ions and oxygen coordination.^[47] The oxidation state of TM ions can be determined by applying a linear combination fit (LCF) on the normalized XANES region. The normalized Ni K-edge and Mn K-edge XANES spectra of LLNMO-PC and LLNMO-SC electrodes during the first charge are exhibited in Figure 5b,c, and Figures S13b,c and S14b,c (Supporting Information). The Ni K-absorption edge of both cathodes clearly shifts towards higher energy until the potential reaches about 4.5 V, demonstrating the oxidation of nickel (II) to close to nickel (IV), (i.e., Ni²⁺ \rightarrow Ni⁴⁺ + 2e⁻). With further charging to the oxygen-involved voltage plateau (≈ 4.6 V), almost no further change in the Ni K-edge energy position can be observed, illustrating that the Ni oxidation state (Ni⁴⁺) does not change significantly in this voltage range. A doublet of two peaks appearing in the pre-edge peaks in the Mn K-edge XANES spectra for both electrodes is observed in Figure 5c, and Figures S13c and S14c (Supporting

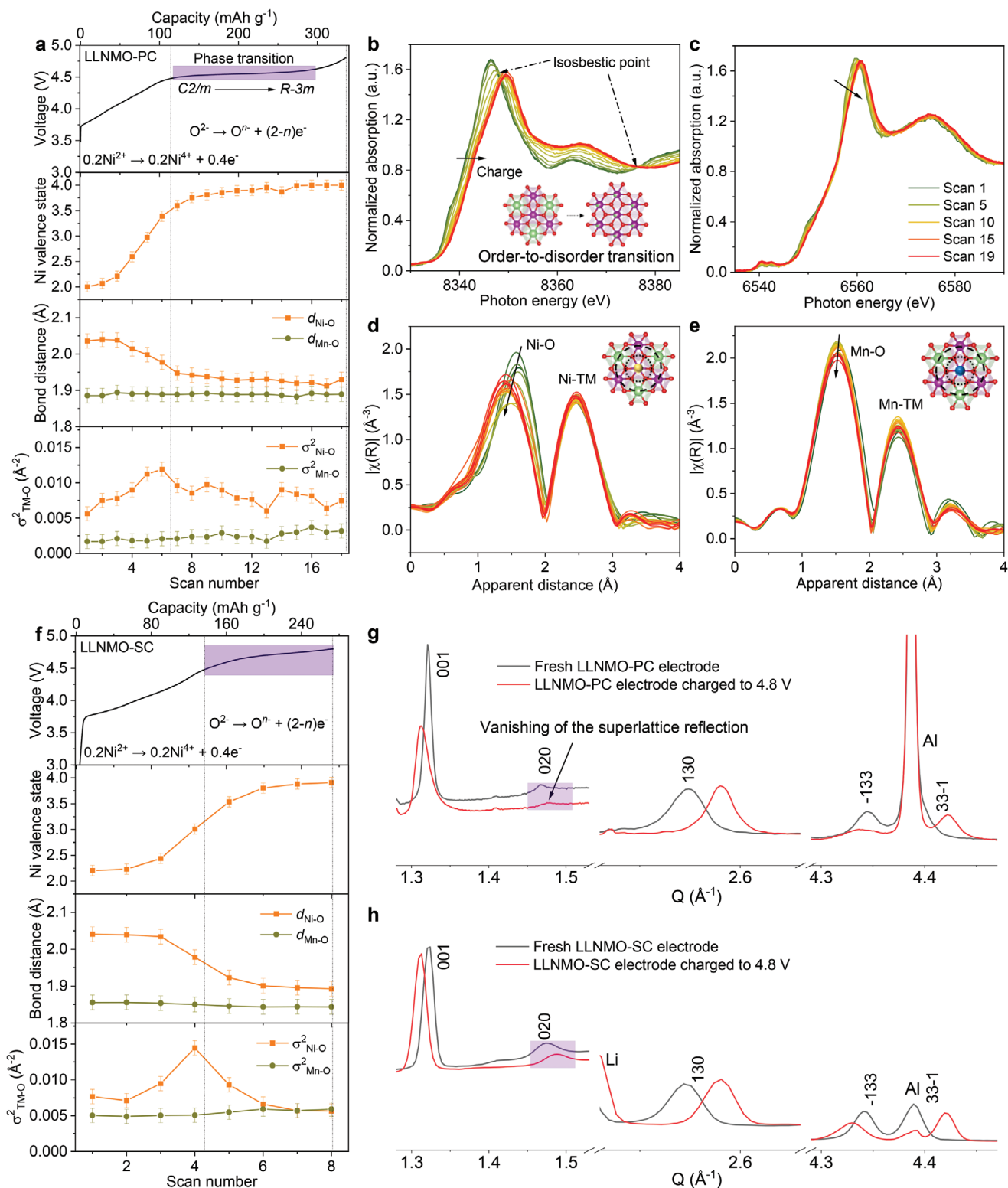


Figure 5. The first charge-voltage profile of a) LLNMO-PC electrodes during in situ XAS experiments; normalized b) Ni and c) Mn K-edge XANES spectra and the Fourier transform magnitudes of k^2 weighted d) Ni and e) Mn K-edge EXAFS spectra for LLNMO-PC; f) the first charge-voltage profile of LLNMO-SC; the sXRD patterns of g) LLNMO-PC and h) LLNMO-SC electrodes before (fresh) and after the first charge to 4.8 V. Quantitative correlations of the capacity with the reaction site are shown in a) and f): evolution of the oxidation of Ni obtained by using LCF method, bond distance, and Debye–Waller factors of Ni–O and Mn–O during the initial charge process.

Information), which is a characteristic of manganese (IV) in oxides. In contrast to Ni, there is no pronounced change in the shape and energy position of Mn K-edge XANES spectra for both electrodes throughout the entire charging process, which suggests that the Mn valence state remains the same as its pristine state (Mn^{4+}) during the initial charging. Therefore, the specific capacity originating from the long plateau at 4.6 V of LLNMO during the first charge can be attributed to the oxidation of lattice oxygen (i.e., $\text{O}^{2-} \rightarrow \text{O}^{n-} + (2 - n) \text{e}^-$, $0 < n < 2$). Very importantly, there are at least two distinct isosbestic points in Ni K-edge XANES spectra of both electrodes from 4.3 V to 4.8 V (Figure 5b, and Figures S13b and S14b, Supporting Information), which hints at a two-phase reaction.^[48]

To determine the local structural variations around the nickel and manganese sites in the LLNMO-PC and the LLNMO-SC electrodes during cycling, the Fourier transform (FT *R*-space) magnitudes of k^2 weighted $\chi(k)$ EXAFS spectra at Mn and Ni K-edges are plotted in Figure 5d,e and Figure S13d,e and S14d,e (Supporting Information). Two distinct peaks are visible in all the FT spectra of both electrodes for Ni and Mn. The first and second coordination spheres at approximately 1.5 and 2.5 Å reflect the scattering interactions of the closest oxygen (i.e., TM–O) and the next-nearest neighboring TM/Li ions within the TM layer in the monoclinic layered structure (i.e., TM–TM) surrounding the absorbing Ni or Mn atoms, respectively, as labeled in each spectrum and shown in the schematic scheme in Figure 5d,e. Note that these values are about 0.3 Å smaller than their actual bond distance because the FT *R*-profiles are not phase-corrected. An apparent change in the position and intensity of the Ni–O peaks is found in both electrodes during the first charging process. A closer inspection reveals that this change is almost completed when the charging voltage reaches around 4.5 V. Afterwards, there are only subtle changes occurring in the Ni–O peak during the activation process. On the other hand, the Mn–O peak of both electrodes only exhibits slight changes throughout the whole charging process. These results indicate that the delithiation reaction of LLNMO cathodes is closely related to the oxidation of Ni in the sloping voltage region (from open-circuit voltage to 4.5 V), and it is mostly related to the variations of oxygen atoms in the high-voltage region.

In order to obtain quantitative information on the local structure of both electrodes, the bond distances (*R*) of TM–O and Debye–Waller factors of the first coordination shells ($\sigma_{\text{Mn-O}}$ and $\sigma_{\text{Ni-O}}$) were obtained by fitting the EXAFS spectra,^[49] see Figure 5a,f and Figures S13a and 14a (Supporting Information). To perform the fitting, a structure model of LiNiO_2 ($R\bar{3}m$) or LiMnO_2 ($R\bar{3}m$) was introduced. Theoretically, the EXAFS Debye–Waller factor σ reflects the static structural disorder (σ_{stat}) and thermal vibrations (σ_{vib}) of the absorbing atoms. Thus, the factors of $\sigma_{\text{Mn-O}}$ and $\sigma_{\text{Ni-O}}$ are indicative of the degree of local structural disorder on Mn and Ni sites in the layered structure. Obviously, the average Ni–O bond distance of LLNMO-PC and LLNMO-SC electrodes shrinks progressively when the charge voltage reaches up to 4.5 V and then stays nearly unchanged as the voltage rises, ranging from 4.5 to 4.8 V, showing that the valence state of Ni-ions is altered from +2 to +4 before 4.5 V and not affected considerably during the voltage plateau at about 4.6 V. Meanwhile, the average Mn–O

distance of both electrodes does not vary significantly with the charge voltage due to an unchanged oxidation state of Mn^{4+} . These results match precisely with the analysis of XANES data described above. Upon the first delithiation, the $\sigma_{\text{Ni-O}}$ factor of both electrodes continues to increase and reaches the maximum value at the end of the sloping voltage (≈ 4.5 V), and declines gradually after charging to voltages higher than 4.6 V. There is only a subtle increase in the $\sigma_{\text{Mn-O}}$ value of both electrodes during the first charge, which is consistent with only a slight change in the $\sigma_{\text{Mn-O}}$ factors for O2-type $\text{Li}_{1.25}\text{Co}_{0.25}\text{Mn}_{0.50}\text{O}_2$ ($P6_3mc$) with a single-layer Li_2MnO_3 superstructure^[50] but different from an enormous variation in the $\sigma_{\text{Mn-O}}$ values previously reported for O3-type $\text{Li}_{1.2}\text{Ni}_{0.15}\text{Co}_{0.1}\text{Mn}_{0.55}\text{O}_2$ cathodes.^[46] This is probably because the prepared $\text{Li}_{1.2}\text{Ni}_{0.2}\text{Mn}_{0.6}\text{O}_2$ oxides are solid solutions with a monoclinic layered structure ($C2/m$) rather than as a composite of nanodomains of rhombohedral layered phase ($R\bar{3}m$) and layered monoclinic phase ($C2/m$). Therefore, it would be reasonable to speculate that the Li-ion extraction induced variations in local structure mainly take place on the Ni and O sites in the layered structure of both electrodes.

Although the changes in the local structure of LLNMO-PC around the Ni and Mn atoms are similar to that of LLNMO-SC during charging, these two electrodes exhibit different levels of long-range cation disorder in the TM layer in the layered structure, as shown in Figure 5g,h. The superlattice reflections such as the 020 reflection in the sXRD patterns of both cathodes can be observed before electrochemical cycling. These reflections of the LLNMO-PC electrode almost disappeared after charging to 4.8 V, which signifies that the superlattice structure is destroyed in LLNMO-PC because of the long-range atomic rearrangement within the TM layer, as confirmed in previous studies.^[43] As a matter of fact, both the rhombohedral layered phase ($R\bar{3}m$) and the monoclinic layered phase ($C2/m$) possess an O3-type structure. Since the in-plane Li/TM or \square /TM (\square for vacancy) ordering on the TM layer in the monoclinic layered structure vanishes gradually during the oxygen activation process, a possible phase transition from the intraplane ordered phase (monoclinic layered structure) to the intraplane disordered phase (rhombohedral layered structure) is proposed, see Figure 6. This could help to explain why the high-voltage plateau of LMLOs at about 4.6 V in the initial charge curve often disappeared on subsequent cycling. Encouragingly, the superstructure reflections in the sXRD pattern of LLNMO-SC cathode are basically maintained when charged up to 4.8 V, which provides solid evidence for the improved structural stability and cycling performance of Li-rich layered cathodes upon long-term cycling.

Furthermore, the morphological changes of both LLNMO-SC and LLNMO-PC electrodes were tracked by SEM and XRD after 100 cycles, as shown in Figures S15 and S16 (Supporting Information). The cracks can be clearly observed in LLNMO-PC (Figure S15d, Supporting Information), which can be ascribed to the anisotropic lattice strain during long-term cycling, see Figure 6. There is no dispute that the fractures would induce the formation of new cathode electrode interphase (CEI) films on the crystal surface, thus resulting in an increased charge transfer resistance and serious voltage fading over cycling. On the contrary, the particle shape of LLNMO-SC is basically maintained after 100 cycles. More importantly, when compared to

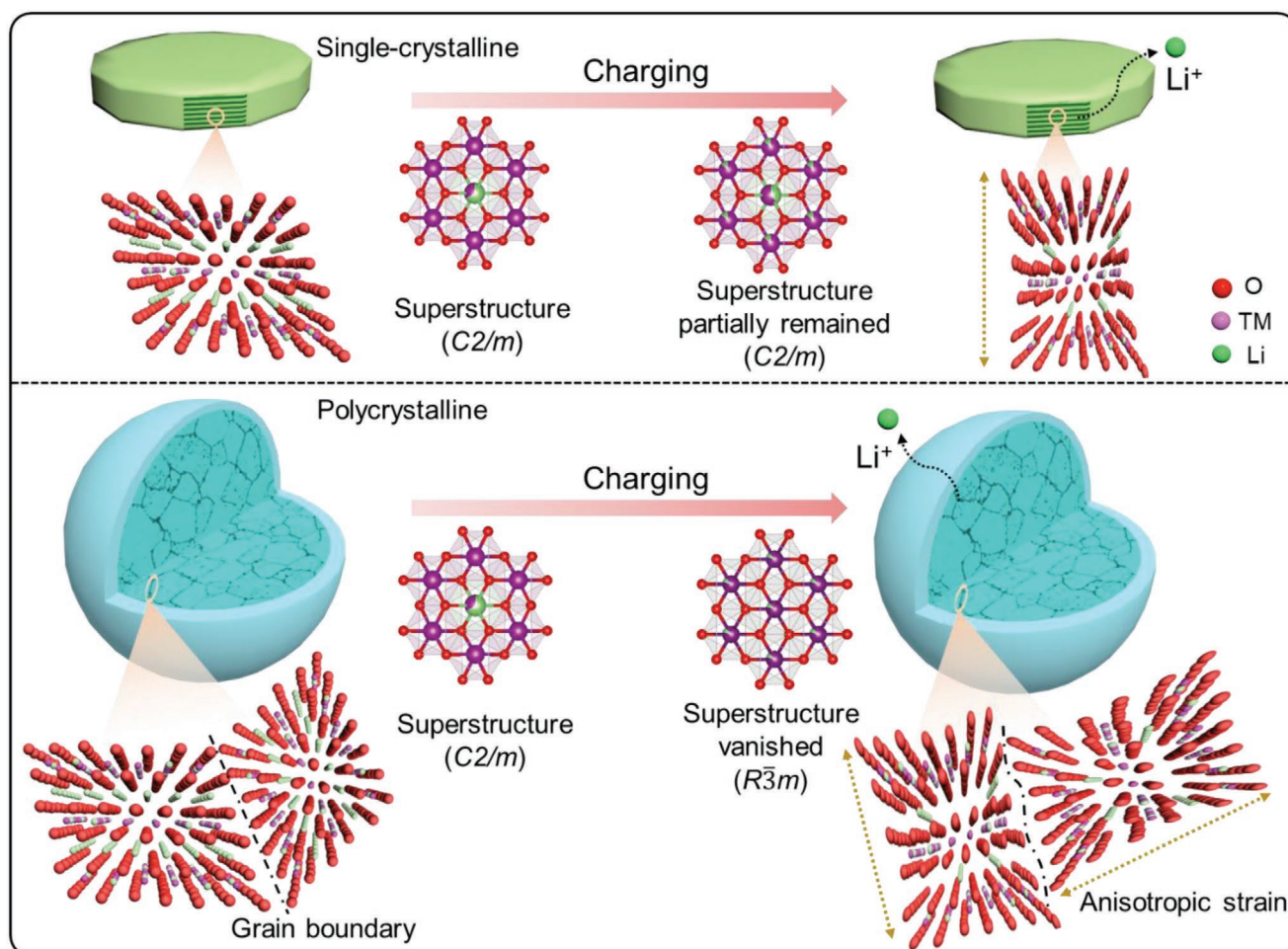


Figure 6. Schematic diagram of the microstructural evolution of LLNMO-SC and LLNMO-PC cathodes during charging, showing a relatively low micro-strain in the LLNMO-SC cathode.

LLNMO-SC, all the reflections in the XRD patterns of LLNMO-PC cathode move significantly to lower scattering angles after 100 cycles (Figure S16b and Table S10, Supporting Information). In other words, there is a strong increase in the unit cell volume for LLNMO-PC (3.0%) in comparison with LLNMO-PC (1.6%).

Finally, high-resolution transmission electron microscopy (HRTEM) was utilized to investigate the surface structural changes of two electrodes after 100 cycles, as exhibited in Figure 7. Figure 7a–e show HRTEM images and fast Fourier transform (FFT) patterns of cycled LLNMO-PC electrode. The measured lattice fringe spacing is approximately 0.47 nm, corresponding to the interslab distance of the (001) plane of the monoclinic layered structure ($C2/m$) or the (003) plane of the rhombohedral layered structure ($R\bar{3}m$). A distorted crystal lattice is clearly observed in both the surface and bulk regions of the LLNMO-PC electrode after extended cycling (see Figure 7a,c,e). Additionally, edge dislocations are also found in the interior part of the cycled LLNMO-PC. In contrast, there is no pronounced lattice distortion and edge dislocation in the aged LLNMO-SC electrode (Figure 7f,h,j). These results provide direct evidence that the LLNMO-PC electrode undergoes large strain resulting from severe lattice distortions upon long-term

cycling, which matches precisely with the in situ XRD results (see Figures 3 and 4). Furthermore, it can be seen from Figure 7e that a large amount of TM migrates to the Li layer on the surface of the cycled LLNMO-PC electrode. Such Li/Ni disorder and lattice distortion can block the diffusion motion of Li ions along the 2D diffusion pathway and thus result in a significant voltage decay and capacity fade in the LLNMO-PC cathode (Figure 2). The corresponding FFT patterns (Figure 7b,d) of the aged LLNMO-PC cathode along the [100] zone axis show an array of points with monoclinic or rhombohedral symmetry ($C2/m$ or $R\bar{3}m$), which are consistent with a layered structure. However, there is no clear evidence for the formation of the spinel phase (AB_2O_4 , $Fd\bar{3}m$) at the surface of the LLNMO-PC crystallites after 100 cycles. Figure 7h,j exhibit lattice fringes with an average d -spacing of around 0.43 nm, corresponding to the (020) plane of the monoclinic layered structure ($C2/m$). An amorphous layer on the LLNMO-SC surface (Figure 7j) indicates the spontaneous formation of cathode electrolyte interphase (CEI) film during long-term cycling. Very importantly, the absence of Li/TM cation disorder on the surface further confirms the structural stability of the LLNMO-SC cathode. The FFT patterns of the cycled LLNMO-SC electrode along the [001] zone axis are in very good agreement with the layered structure.

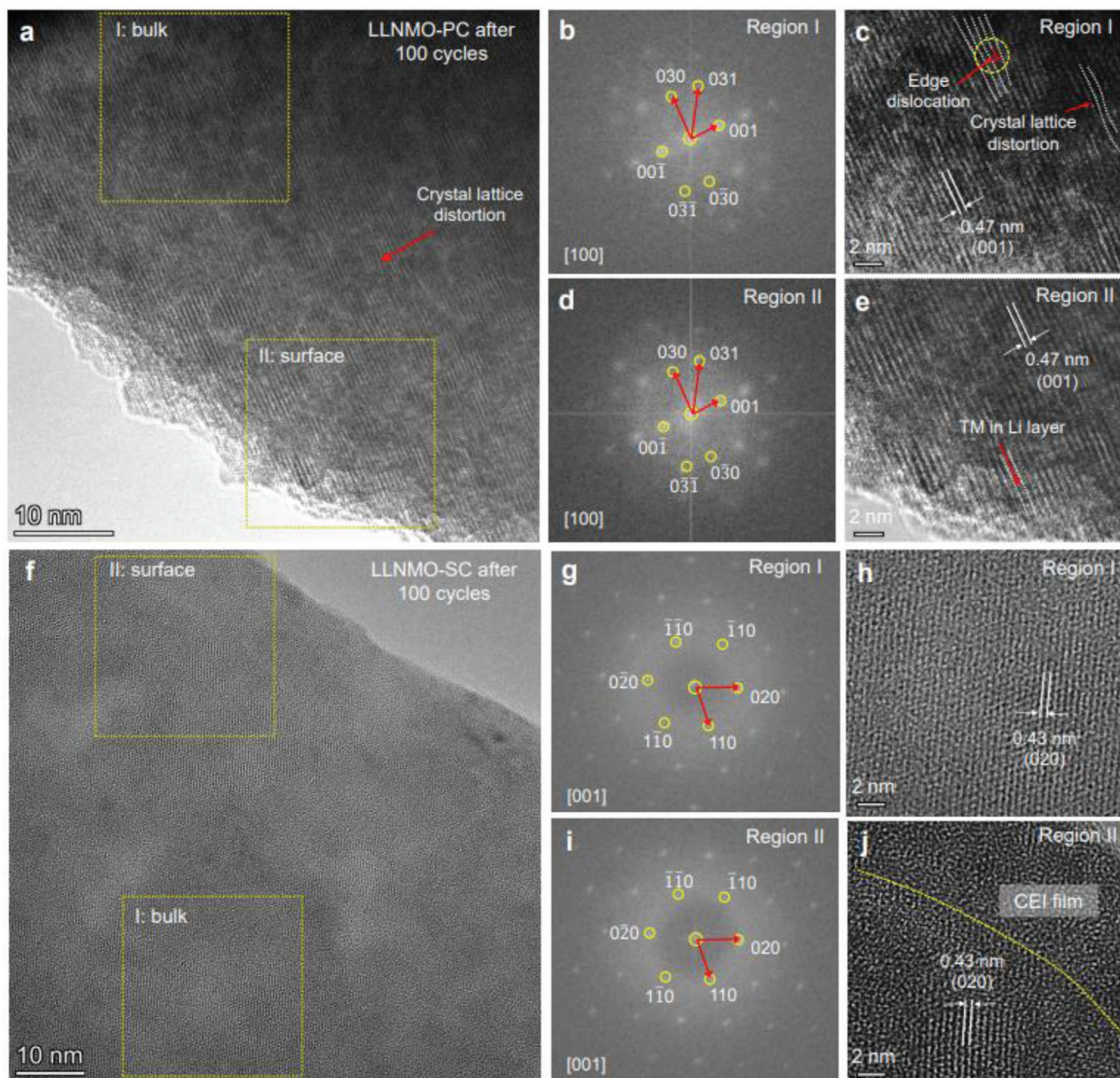


Figure 7. HRTEM images of a,c,e) LLNMO-PC and f,h,i) LLNMO-SC electrodes after 100 cycles and the corresponding FFT patterns of b,d) LLNMO-PC and g,i) LLNMO-SC electrodes.

Besides, no TM ions located on tetrahedral sites can be found in the aged LLNMO-SC cathode, pointing out that the Li-poor spinel phase (AB_2O_4 , $Fd\bar{3}m$) was not formed after 100 cycles. Therefore, these results unambiguously confirm that morphology regulation could effectively enhance the structural stability and mitigate the voltage degradation of LLNMO.

3. Conclusion

In summary, the monoclinic layered LLNMO-SC ($C2/m$) with an average particle diameter of about $1\ \mu\text{m}$ was successfully synthesized via a Li^+/Na^+ ion-exchange method. A cathode made of

the prepared LLNMO-SC delivers an outstanding cycling performance, demonstrating capacity retention of nearly 100% after 100 cycles at 0.1 C between 2.0 and 4.8 V. More interestingly, the severe voltage decay can be effectively suppressed in the LLNMO-SC electrode when compared with the typical polycrystalline $\text{Li}[\text{Li}_{0.2}\text{Ni}_{0.2}\text{Mn}_{0.6}]\text{O}_2$ electrode. The structural changes and charge compensation mechanisms for both LLNMO-SC and LLNMO-PC during Li-ion deintercalation and intercalation have been systematically investigated using in situ sXRD and XAS techniques. It is observed that, in contrast to LLNMO-PC, a slight change in lattice parameters and small microstructural strain can be realized in LLNMO-SC upon cycling, which contributes to enhanced structural stability and alleviates the

voltage fading during long-term cycling. Both in situ XANES spectra and high-resolution ex situ sXRD results suggest that the oxygen-related plateau of LLNMO located at about 4.6 V during the first charge is associated with a phase transition from a monoclinic layered structure ($C2/m$) to a rhombohedral layered structure ($R\bar{3}m$). Faster reaction kinetics for Ni upon cycling is uncovered by in situ XAS experiments, but the local structure around Mn atoms in LLNMO is only minimally affected by Li-ion extraction/insertion. These findings not only offer an effective approach to engineering the single-crystalline Li-rich cathode materials with good performance, but also provide new insights into the structural degradation of LMLOs.

Supporting Information

Supporting Information is available from the Wiley Online Library or from the author.

Acknowledgements

W.H. acknowledges the National Science Foundation of China (grant no. 22108218) and “Young Talent Support Plan” of Xi’an Jiaotong University (71211201010723). This work was financially supported by the Guangxi Science and Technology Base and Talents Special Project (Grant No. AD21159007), the Natural Science Foundation of Guangxi (Grant No. 2020GXNSFBFA297029), the Foundation of Key Laboratory of New Processing Technology for Nonferrous Metal & Materials, Ministry of Education/Guangxi Key Laboratory of Optical and Electronic Materials and Devices, Guilin University of Technology (Contract No. 20AA-13). The TEM characterization experiments were performed at the Karlsruhe Nano Micro Facility (KNMF), a Helmholtz research infrastructure operated at KIT. The authors acknowledge DESY (Hamburg, Germany), a member of the Helmholtz Association HGF, for the provision of experimental facilities. This work contributes to the research performed at CELEST (Center for Electrochemical Energy Storage Ulm-Karlsruhe) and was supported by the German Research Foundation (DFG) under Project ID 390874152 (POLiS Cluster of Excellence).

Open access funding enabled and organized by Projekt DEAL.

Conflict of Interest

The authors declare no conflict of interest.

Author Contributions

W.H. conceived the idea and discussed with X.Y., S.W., J.S. H.E and S.I.; X.Y., D.H. and S.W. carried out the preparation experiments; W.H., A.T., V.B. A.M. and F.Q. performed the synchrotron-based and laboratory X-ray diffraction measurements; K.W. performed the TEM experiments; the data were analyzed by X.Y., W.H. and S.W.; X.Y., W.H., and S.W. wrote the preliminary draft with input from S.I and H.E.; all authors revised the manuscript and have given the approval to the final version of the manuscript.

Data Availability Statement

The data that support the findings of this study are available on request from the corresponding author. The data are not publicly available due to privacy or ethical restrictions.

Keywords

in situ synchrotron-based techniques, Li- and Mn-rich cathode materials, single crystals, structural stability, voltage decay

Received: March 9, 2022

Revised: May 8, 2022

Published online: May 23, 2022

- [1] W. Li, E. M. Erickson, A. Manthiram, *Nat. Energy* **2020**, *5*, 26.
- [2] R. A. House, U. Maitra, M. A. Pérez-Osorio, J. G. Lozano, L. Jin, J. W. Somerville, L. C. Duda, A. Nag, A. Walters, K. J. Zhou, M. R. Roberts, P. G. Bruce, *Nature* **2020**, *577*, 502.
- [3] Y. Bi, J. Tao, Y. Wu, L. Li, Y. Xu, E. Hu, B. Wu, J. Hu, C. Wang, J.-G. Zhang, Y. Qi, J. Xiao, *Science* **2020**, *370*, 1313.
- [4] S. Saha, G. Assat, M. T. Sougrati, D. Foix, H. Li, J. Vergnet, S. Turi, Y. Ha, W. Yang, J. Cabana, G. Rousse, A. M. Abakumov, J. M. Tarascon, *Nat. Energy* **2019**, *4*, 977.
- [5] X. Li, Y. Qiao, S. Guo, Z. Xu, H. Zhu, X. Zhang, Y. Yuan, P. He, M. Ishida, H. Zhou, *Adv. Mater.* **2018**, *30*, 1705197.
- [6] P. Liu, H. Zhang, W. He, T. Xiong, Y. Cheng, Q. Xie, Y. Ma, H. Zheng, L. Wang, Z. Z. Zhu, Y. Peng, L. Mai, D. L. Peng, *J. Am. Chem. Soc.* **2019**, *141*, 10876.
- [7] W. Hua, S. Wang, M. Knapp, S. J. Leake, A. Senyshyn, C. Richter, M. Yavuz, J. R. Binder, C. P. Grey, H. Ehrenberg, S. Indris, B. Schwarz, *Nat. Commun.* **2019**, *10*, 5365.
- [8] A. Grenier, G. E. Kamm, Y. Li, H. Chung, Y. S. Meng, K. W. Chapman, *J. Am. Chem. Soc.* **2021**, *143*, 5763.
- [9] W. Zuo, M. Luo, X. Liu, J. Wu, H. Liu, J. Li, M. Winter, R. Fu, W. Yang, Y. Yang, *Energy Environ. Sci.* **2020**, *13*, 4450.
- [10] P. E. Pearce, A. J. Perez, G. Rousse, M. Saubanère, D. Batuk, D. Foix, E. McCalla, A. M. Abakumov, G. Van Tendeloo, M. L. Doublet, J. M. Tarascon, *Nat. Mater.* **2017**, *16*, 580.
- [11] J. Hu, W. Li, Y. Duan, S. Cui, X. Song, Y. Liu, J. Zheng, Y. Lin, F. Pan, *Adv. Energy Mater.* **2017**, *7*, 1601894.
- [12] Y. Orikasa, T. Maeda, Y. Koyama, H. Murayama, K. Fukuda, H. Tanida, H. Arai, E. Matsubara, Y. Uchimoto, Z. Ogumi, *Chem. Mater.* **2013**, *25*, 1032.
- [13] D. Tang, Y. Sun, Z. Yang, L. Ben, L. Gu, X. Huang, *Chem. Mater.* **2014**, *26*, 3535.
- [14] Y. Qiao, Z. Zhou, Z. Chen, S. Du, Q. Cheng, H. Zhai, N. J. Fritz, Q. Du, Y. Yang, *Nano Energy* **2018**, *45*, 68.
- [15] L. De Biasi, B. Schwarz, T. Brezesinski, P. Hartmann, J. Janek, H. Ehrenberg, *Adv. Mater.* **2019**, *31*, 1900985.
- [16] W. Hua, B. Schwarz, M. Knapp, A. Senyshyn, A. Missiul, X. Mu, S. Wang, C. Kübel, J. R. Binder, S. Indris, H. Ehrenberg, *J. Electrochem. Soc.* **2019**, *166*, A5025.
- [17] W. Hua, B. Schwarz, R. Azmi, M. Müller, M. S. Dewi Darma, M. Knapp, A. Senyshyn, M. Heere, A. Missyul, L. Simonelli, J. R. Binder, S. Indris, H. Ehrenberg, *Nano Energy* **2020**, *78*, 105231.
- [18] H. Yu, Y. Cao, L. Chen, Y. Hu, X. Duan, S. Dai, C. Li, H. Jiang, *Nat. Commun.* **2021**, *12*, 4564.
- [19] W. Hua, M. Chen, B. Schwarz, M. Knapp, M. Bruns, J. Barthel, X. Yang, F. Sigel, R. Azmi, A. Senyshyn, A. Missiul, L. Simonelli, M. Etter, S. Wang, X. Mu, A. Fiedler, J. R. Binder, X. Guo, S. Chou, B. Zhong, S. Indris, H. Ehrenberg, *Adv. Energy Mater.* **2019**, *9*, 1803094.
- [20] D. Eum, B. Kim, S. J. Kim, H. Park, J. Wu, S. P. Cho, G. Yoon, M. H. Lee, S. K. Jung, W. Yang, W. M. Seong, K. Ku, O. Tamwattana, S. K. Park, I. Hwang, K. Kang, *Nat. Mater.* **2020**, *19*, 419.
- [21] M. Sathiy, A. M. Abakumov, D. Foix, G. Rousse, K. Ramesha, M. Saubanère, M. L. Doublet, H. Vezin, C. P. Laisa, A. S. Prakash, D. Gonbeau, G. Vantendeloo, J. M. Tarascon, *Nat. Mater.* **2015**, *14*, 230.

- [22] S. Myeong, W. Cho, W. Jin, J. Hwang, M. Yoon, Y. Yoo, G. Nam, H. Jang, J. G. Han, N. S. Choi, M. G. Kim, J. Cho, *Nat. Commun.* **2018**, *9*, 3285.
- [23] W. Hua, K. Wang, M. Knapp, B. Schwarz, S. Wang, H. Liu, J. Lai, M. Müller, A. Schökel, A. Missyul, D. Ferreira Sanchez, X. Guo, J. R. Binder, J. Xiong, S. Indris, H. Ehrenberg, *Chem. Mater.* **2020**, *32*, 4984.
- [24] S. T. Myung, F. Maglia, K. J. Park, C. S. Yoon, P. Lamp, S. J. Kim, Y. K. Sun, *ACS Energy Lett.* **2017**, *2*, 196.
- [25] C. S. Yoon, S. J. Kim, U. H. Kim, K. J. Park, H. H. Ryu, H. S. Kim, Y. K. Sun, *Adv. Funct. Mater.* **2018**, *28*, 1802090.
- [26] S. Wang, W. Hua, A. Missyul, M. S. D. Darma, A. Tayal, S. Indris, H. Ehrenberg, L. Liu, M. Knapp, *Adv. Funct. Mater.* **2021**, *31*, 2009949.
- [27] W. Hua, X. Yang, N. P. M. Casati, L. Liu, S. Wang, V. Baran, M. Knapp, H. Ehrenberg, S. Indris, *eScience* **2022**, *2*, 183.
- [28] W. Hua, W. Liu, M. Chen, S. Indris, Z. Zheng, X. Guo, M. Bruns, T. H. Wu, Y. Chen, B. Zhong, S. Chou, Y. M. Kang, H. Ehrenberg, *Electrochim. Acta* **2017**, *232*, 123.
- [29] J. N. Clark, J. Ihli, A. S. Schenk, Y. Y. Kim, A. N. Kulak, J. M. Campbell, G. Nisbet, F. C. Meldrum, I. K. Robinson, *Nat. Mater.* **2015**, *14*, 780.
- [30] S. Li, Z. Jiang, J. Han, Z. Xu, C. Wang, H. Huang, C. Yu, S. J. Lee, P. Pianetta, H. Ohldag, J. Qiu, J. S. Lee, F. Lin, K. Zhao, Y. Liu, *Nat. Commun.* **2020**, *11*, 4433.
- [31] G. L. Xu, Q. Liu, K. K. S. Lau, Y. Liu, X. Liu, H. Gao, X. Zhou, M. Zhuang, Y. Ren, J. Li, M. Shao, M. Ouyang, F. Pan, Z. Chen, K. Amine, G. Chen, *Nat. Energy* **2019**, *4*, 484.
- [32] Y. Mao, X. Wang, S. Xia, K. Zhang, C. Wei, S. Bak, Z. Shadike, X. Liu, Y. Yang, R. Xu, P. Pianetta, S. Ermon, E. Stavitski, K. Zhao, Z. Xu, F. Lin, X. Q. Yang, E. Hu, Y. Liu, *Adv. Funct. Mater.* **2019**, *29*, 1900247.
- [33] E. Trevisanello, R. Ruess, G. Conforto, F. H. Richter, J. Janek, *Adv. Energy Mater.* **2021**, *11*, 2003400.
- [34] P. Yan, J. Zheng, M. Gu, J. Xiao, J. G. Zhang, C. M. Wang, *Nat. Commun.* **2017**, *8*, 14101.
- [35] P. Yan, J. Zheng, Z. K. Tang, A. Devaraj, G. Chen, K. Amine, J. G. Zhang, L. M. Liu, C. Wang, *Nat. Nanotechnol.* **2019**, *14*, 602.
- [36] A. R. Armstrong, M. Holzapfel, P. Nová, C. S. Johnson, S.-H. Kang, M. M. Thackeray, P. G. Bruce, *J. Am. Chem. Soc.* **2006**, *128*, 8694.
- [37] E. Hu, X. Yu, R. Lin, X. Bi, J. Lu, S. Bak, K. W. Nam, H. L. Xin, C. Jaye, D. A. Fischer, K. Amine, X. Q. Yang, *Nat. Energy* **2018**, *3*, 690.
- [38] T. Deng, X. Fan, L. Cao, J. Chen, S. Hou, X. Ji, L. Chen, S. Li, X. Zhou, E. Hu, D. Su, X. Q. Yang, C. Wang, *Joule* **2019**, *3*, 2550.
- [39] K. Kang, Y. S. Meng, J. Bréger, C. P. Grey, G. Ceder, *Science* **2006**, *311*, 977.
- [40] X. Cao, H. Li, Y. Qiao, M. Jia, P. He, J. Cabana, H. Zhou, *Energy Storage Mater.* **2021**, *38*, 1.
- [41] W. Hua, S. Wang, K. Wang, A. Missyul, Q. Fu, M. S. Dewi Darma, H. Li, V. Baran, L. Liu, C. Kübel, J. R. Binder, M. Knapp, H. Ehrenberg, S. Indris, *Chem. Mater.* **2021**, *33*, 5606.
- [42] J. Sun, C. Sheng, X. Cao, P. Wang, P. He, H. Yang, Z. Chang, X. Yue, H. Zhou, *Adv. Funct. Mater.* **2021**, *32*, 2110295.
- [43] R. A. House, G. J. Rees, M. A. Pérez-Osorio, J. J. Marie, E. Boivin, A. W. Robertson, A. Nag, M. Garcia-Fernandez, K. J. Zhou, P. G. Bruce, *Nat. Energy* **2020**, *5*, 777.
- [44] K. Luo, M. R. Roberts, R. Hao, N. Guerrini, D. M. Pickup, Y. S. Liu, K. Edström, J. Guo, A. v. Chadwick, L. C. Duda, P. G. Bruce, *Nat. Chem.* **2016**, *8*, 684.
- [45] J. L. Shi, J. N. Zhang, M. He, X. D. Zhang, Y. X. Yin, H. Li, Y. G. Guo, L. Gu, L. J. Wan, *ACS Appl. Mater. Interfaces* **2016**, *8*, 20138.
- [46] X. Yu, Y. Lyu, L. Gu, H. Wu, S. M. Bak, Y. Zhou, K. Amine, S. N. Ehrlich, H. Li, K. W. Nam, X. Q. Yang, *Adv. Energy Mater.* **2014**, *4*, 1300950.
- [47] H. Li, W. Hua, X. Liu-Théato, Q. Fu, M. Desmau, A. Missyul, M. Knapp, H. Ehrenberg, S. Indris, *Chem. Mater.* **2021**, *33*, 9546.
- [48] S. Zhao, C. Tan, C. T. He, P. An, F. Xie, S. Jiang, Y. Zhu, K. H. Wu, B. Zhang, H. Li, J. Zhang, Y. Chen, S. Liu, J. Dong, Z. Tang, *Nat. Energy* **2020**, *5*, 881.
- [49] M. Newville, *J. Synchrotron Rad.* **2001**, *8*, 96.
- [50] Y. Zuo, B. Li, N. Jiang, W. Chu, H. Zhang, R. Zou, D. Xia, *Adv. Mater.* **2018**, *30*, 1707255.